Journal of Engineering Science and Technology
Vol. 18, No. 1 (2023) 437 - 452

MORPHOLOGICAL, STRUCTURAL, AND PHOTOLUMINESCENCE PROPERTIES OF Er^{3+}-DOPED SiO_2-ZrO_2/PVA NANOFIBER

NURUL FASIHAH MOHD SUHAIMI,
SURAYA AHMAD KAMIL*, MOHD KAMIL ABD RAHMAN

Faculty of Applied Sciences, Universiti Teknologi MARA,
40450 Shah Alam, Selangor, Malaysia
*Corresponding Author: suraya_ak@uitm.edu.my

Abstract

The effect of the combination of glass and ceramic of the fabricated nanofibers on the morphological, structural, and photoluminescence properties has been evaluated. Sol-gel and electrospinning techniques were used to fabricate Er^{3+}-doped SiO_2-ZrO_2/PVA nanofibers with varying concentrations of SiO_2 and ZrO_2. The nanofiber diameter ranged from 130 nm to 390 nm depending on the zirconia concentration and calcination temperature. The optimum concentration of the solution for electrospun fibers is important to stabilize the fibrous gel. The X-ray diffraction (XRD) intensity increased with increasing ZrO_2 content, indicating the enhanced crystallinity of the nanofibers. The tetragonal phase at low temperatures can be attributed to the presence of rare-earth doping. The embedded ZrO_2 nanocrystal in the amorphous SiO_2 matrix contributed to the narrow photoluminescence emission. Er^{3+} luminescence is more intense in the higher content of ZrO_2 samples. The variation of the peak intensity in Fourier transform infrared (FTIR) spectra indicates the inclusion of ZrO_2 content can alter the rigidity and connectivity of the SiO_2 matrix. The absence of the OH- group in the FTIR spectra indicates that nanofibers have undergone complete densification.

Keywords: Glass-ceramic, Nanofiber, Optical materials, Photoluminescence, Rare-earth.

1. Introduction

Binary silica-zirconia (SiO_2-ZrO_2) has received tremendous attention because of its superior electronic, mechanical, catalytic and thermal, characteristics [1]. SiO_2-ZrO_2 has been utilized in fibres [2], catalysts [3], glasses [4] and coatings [5]. These glasses can easily be crystallized and form glass-ceramic (GC) with embedded ZrO_2 crystals after being annealed [6]. This GC combination has many good features, such as high thermal shock resistance, low defects, high hardness and easy fabrication; in addition, it can be moulded into a complicated shape. Unlike calcined ceramics, GCs are mostly free from porosity. The presence of the crystalline phase in the glass network can enhance the existing characteristic or produces new properties [7].

The addition of erbium ion in GC is beneficial to photonic devices particularly optical amplifiers and solid state lasers due to its ability to emit narrow emission lines caused by an electronic transition in the $4f^n$ band [8]. The unique properties of Er^{3+} ion have made this rare-earth ion an active constituent material in modern optical technology, especially in telecommunication systems because the ion-ion transition that radiates at 1550 nm coincides with minimal loss in the absorption spectrum of single-mode optical fibers [9]. Er^{3+} ion transition also emits photon energy in the visible (red, green and blue) spectral region for several applications [10, 11]. Furthermore, on the same chip, Er^{3+}-doped dielectric thin film has the potential to be employed to create lasers or optical amplifiers which can be combined with other devices [12]. The optical properties of Er^{3+} ion doped GC can be altered by adjusting the content of Er^{3+} ion embedded in the GC host matrix.

Considerable efforts have been exerted to increase photoluminescence emission. A previous study showed that quantum dots and nanostructured materials can produce large effective Stokes shifts, broad absorption and narrow photoluminescence with high quantum yield [13]. One-dimensional nanostructures, such as nanofibers have diameters ranging from 1 nm to 1 μm and an aspect ratio (length/diameter) larger than 100:1 [14].

The emergence of nanotechnology with photonics is incited by the increasing demand for the integration of photonic devices for many applications, including quick response, high data transmission rates, dense data storage and low power consumption [15, 16]. Moreover, nanofibers have several applications, such as in tissue engineering, drug delivery, wound dressings, filtration, and biosensor [17], owing to their outstanding properties, such as high pore volume, high surface area and small pore size.

Fabrication of rare-earth doped nanofibers for applications in luminescence devices has attracted considerable attention due to their higher luminescence intensity than films and bulk powders in recent years [18, 19]. Aside from improving the material properties, ultra-fine composite nanofibers that contain a smaller size of diameter and large area-to-volume ratio can also create a new characteristic that cannot be observed in bulk materials [20].

Since the photoluminescence properties of Er^{3+} with optimum optical properties of the host are concerned, one-dimensional nanofibers fabricated using electrospinning technique have been developed. The present study aims to investigate the morphological, structural and photoluminescence properties of Er^{3+}-doped SiO_2-ZrO_2/PVA nanofibers fabricated using electrospinning technique.

2. Methodology

2.1. Er^{3+}-doped SiO_2-ZrO_2/PVA solution preparation

Er^{3+}-doped SiO_2-ZrO_2/PVA solution was prepared using the sol-gel technique. First, ethanol (EtOH), ultra-pure water (H_2O), hydrochloric acid (HCl) and tetraethylorthosilicate (TEOS) with a molar ratio of 37.9: 2: 0.01: 1 were mixed to prepare a SiO_2 solution. HCl and EtOH were added as a catalyst and solvent, respectively. The mixture was magnetically stirred at 60 °C for 1 h at 500 rpm. Then, zirconium oxychlorideoctahydrate ($ZrOCl_2$. $8H_2O$) was mixed with EtOH to prepare the ZrO_2 solution. The SiO_2 solution was added into ZrO_2 solution followed by 0.58 mol% $ErCl_3 \cdot 6H_2O$. The mixture solution was then stirred at 500 rpm for 16 h at room temperature to ensure that the overall solution become homogenous and transparent. Then, a polyvinyl alcohol (PVA) solution was added into the resultant solution. The experiment was carried out with five samples on different molar ratios of SiO_2-ZrO_2, including 30-70 (3S7Z), 40-60 (4S6Z), 50-50 (5S5Z), 60-40 (6S4Z) and 70-30 (3S7Z), doped with 0.58 mol% of Er^{3+}.

2.2. Nanofiber fabrication

Nanofibers were fabricated using a stand-alone NE-1000 Programmable Single Syringe Pump. Figure 1 depicts the schematic of the electrospinning equipment. The Er-doped SiO_2-ZrO_2/PVA solution was filled into a 3 mL syringe with stainless steel needle attached and placed on a programmable syringe pump. Then, the feed rate of the syringe pump to extrude the solution was 0.6 mL/h. The nanofibers were fabricated when 12 kV of the applied voltage was subjected between the needle tip and the collector. The distance between the needle tip and the drum collector was 10 cm. Aluminium foil was used to cover the drum collector, and a fused silica substrate was attached to it. The resultant nanofibers were calcined for 1 h at 900 °C at a heating rate of 1°C/min.

2.3. Sample characterization

A viscometer (Brookfield) was used to determine the Er^{3+}-doped SiO_2-ZrO_2/PVA solution viscosity. Energy dispersive X-ray (EDX) was employed to identify the presence of chemical elements in the nanofibers. The morphology of the fabricated nanofibers was observed using Field emission scanning electron microscopy (FESEM) (SUPRA40VP). Fourier transform infrared (FTIR) spectrometry (PerkinElmer Spectrum One, Massachusetts, United States) was employed to determine the infrared transmittance spectra. The crystallinity of the samples was investigated using X-ray diffraction (XRD) (PANalytical X'pert PRO, Almelo, Netherlands). Photo-luminescence spectra in the visible range were collected using Horiba Jobin Yvon spectrophotometer with argon laser (514 nm) as an excitation source.

3. Results and Discussion

Electrospun nanofibers morphology of the Er^{3+}-doped $40SiO_2$-$60ZrO_2$/PVA with PVA concentrations of 7, 8, 9 and 10 wt% is shown in Fig. 2. All the nanofibers possessed smooth and cylindrical morphologies with random orientation. Polyvinyl alcohol (PVA) was added to this solution to produce continuous nanofibers by increasing the amount of polymer entanglement in the nanofiber solution [21]. PVA affects the viscosity of the solution. Thus, PVA with different weight concentrations

was added into Er^{3+}-doped $40SiO_2$-$60ZrO_2$ solution to investigate the best proportion of PVA to prepare smooth and uniform electrospun fibers. During electrospinning, solution viscosity is an important parameter because it can influence the nanofiber morphology. Defects such as breakage, branching and beads can occur because of unsuitable solution viscosity during electrospinning [22, 23].

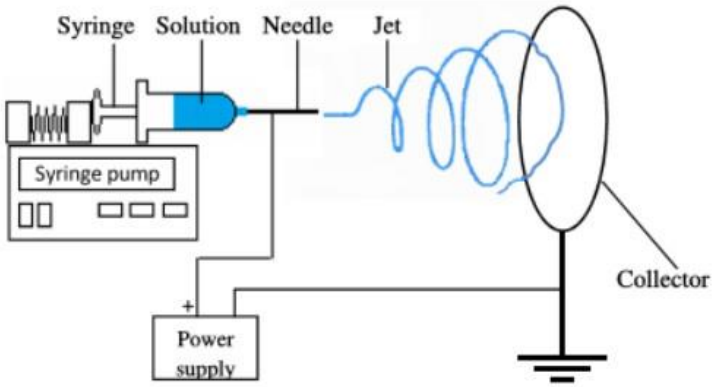

Fig. 1. Schematic of electrospinning setup.

The average diameters of Er^{3+}-doped $40SiO_2$-$60ZrO_2$/PVA nanofibers with various weight percentages of PVA and viscosity are presented in Table 1. The average diameter of the electrospun nanofibers is affected by the PVA concentration and viscosity. The solution concentration significantly affected the structural morphology and fiber diameter. At a low concentration of 7 wt% PVA, the structural morphology varied between cylindrical and flat ribbon fibers. The fibers also merged to form webs and small regions of solidified solution. At 8 wt% PVA, these fibers were smooth with some of the fibers merging to form a single large fiber and flat ribbon fibers. The number of defects declined as the PVA concentration increased. This phenomenon led to the formation of uniform and cylindrical fibers. The viscoelastic forces improved with increasing solution concentration, which helped increase the polymer chain entanglement and led to the creation of smooth and uniform fibers [24]. During electrospinning, there is optimum concentration of the solution for electrospun fibers in order to stabilize the fibrous gel.

The diameter of the electrospun Er^{3+}-doped $40SiO_2$-$60ZrO_2$/PVA nanofibers increased with increasing PVA concentration from 7 to 9 wt%, as shown in Table 1. This result can be ascribed to the increasing viscosity of the solution. The solution viscosity increased with increasing PVA solution, which enhanced the chain entanglements and allowed the jet to lengthen further during its flight. In addition, the fibers were stabilized at higher solution concentrations. However, the diameter of the electrospun nanofiber significantly decreased at 10 wt% PVA. This result can be ascribed to the fact that the fibers are difficult to form at viscosities above 3000 centipoises because the solution is drying at the needle tip [25]. Thus, after approximately 30 min of electrospinning, the mixture started to block the nozzle of the needle and thin fibers hindered the large fiber diameter, which resulted in the formation of small average fiber diameters.

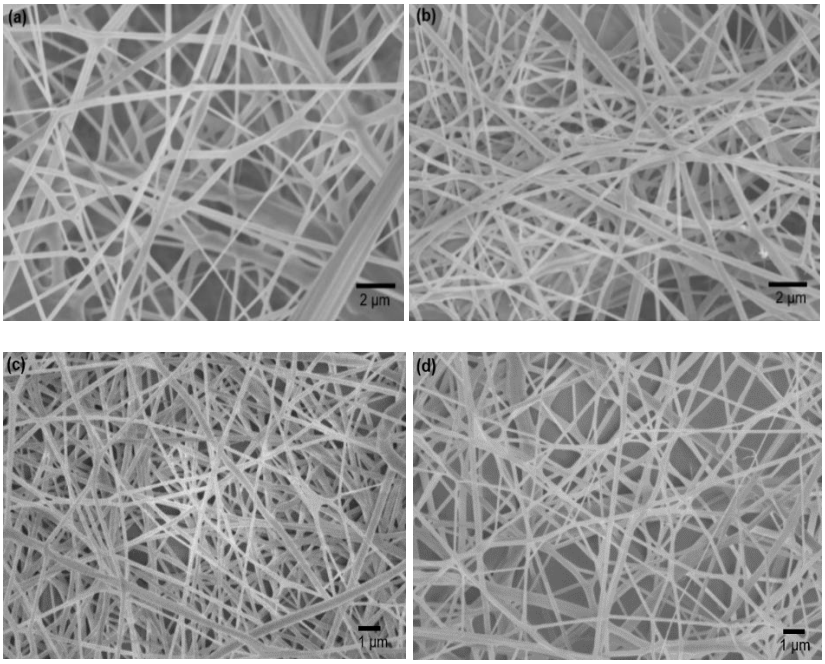

Fig. 2. FESEM images of Er^{3+}-doped $40SiO_2$-$60ZrO_2$ mixed with (a) 7 wt%, (b) 8 wt%, (c) 9wt% and (d) 10 wt% PVA.

Table 1. Average diameter of Er^{3+}-doped $40SiO_2$-$60ZrO_2$/PVA nanofibers with various weight percentages of PVA.

PVA concentration in $40SiO_2$-$60ZrO_2$ doped with Er^{3+} (wt.%)	Viscosity (cPs)	Average diameter of nanofiber (nm)
7 wt%	451.67	255 ± 75
8 wt%	892.50	328 ± 98
9 wt%	1757.50	340 ± 110
10 wt%	3226.67	250 ± 72

Since the nanofibers fabricated by a PVA 9 wt% solution are smoother and has a more uniform surface, this PVA concentration was selected to study the effect of various concentrations of SiO_2 and ZrO_2. The morphology of the Er^{3+}-doped SiO_2-ZrO_2/PVA nanofibers with various concentrations of SiO_2 and ZrO_2 is shown in Fig. 3. The micrographs showed the random orientation of the electrospun nanofibers. The average diameters of the as-spun and calcined (600 °C) nanofibers ranges from 196 nm to 324 nm and 133 nm to 209 nm, respectively as listed in Table 2. Heat treatment caused the dimension and morphology of the calcined nanofibers at 600 °C were different from those of the as-spun nanofibers. After calcination, the surface morphology of the nanofibers was well preserved and exhibited shrinkages with average diameters reduced by approximately 25%. These phenomena can be ascribed to the removal of organic compounds and decomposition of PVA during calcination process as the PVA polymers decomposed above 300 °C [26].

Table 2. Average diameter of SiO_2-ZrO_2/PVA doped with Er^{3+} for as-spun and calcined nanofiber.

Molar ratios of SiO_2:ZrO_2 in 9 wt% of PVA	Average diameter of nanofiber	
	As-spun nanofibers at 100 °C (nm)	Calcined nanofibers at 600 °C (nm)
$30SiO_2$-$70ZrO_2$	196 ± 38	133 ± 29
$40SiO_2$-$60ZrO_2$	278 ± 89	196 ± 51
$50SiO_2$-$50ZrO_2$	283 ± 90	209 ± 40
$60SiO_2$-$40ZrO_2$	324 ± 93	156 ± 43
$70SiO_2$-$30ZrO_2$	267 ± 85	157 ± 40

The elemental composition of the calcinated Er^{3+}-doped $40\%SiO_2$-$60\%ZrO_2$ fibres, is reported in Fig. 4. It has been confirmed that the resulting nanofiber does contain desired elements of C, O, Si, Zr and Er. The presence of carbon elements was due to the alkyl groups from the precursor. The peaks belonging to Au originated from the alloy paste used for coating the calcined samples for FESEM viewing.

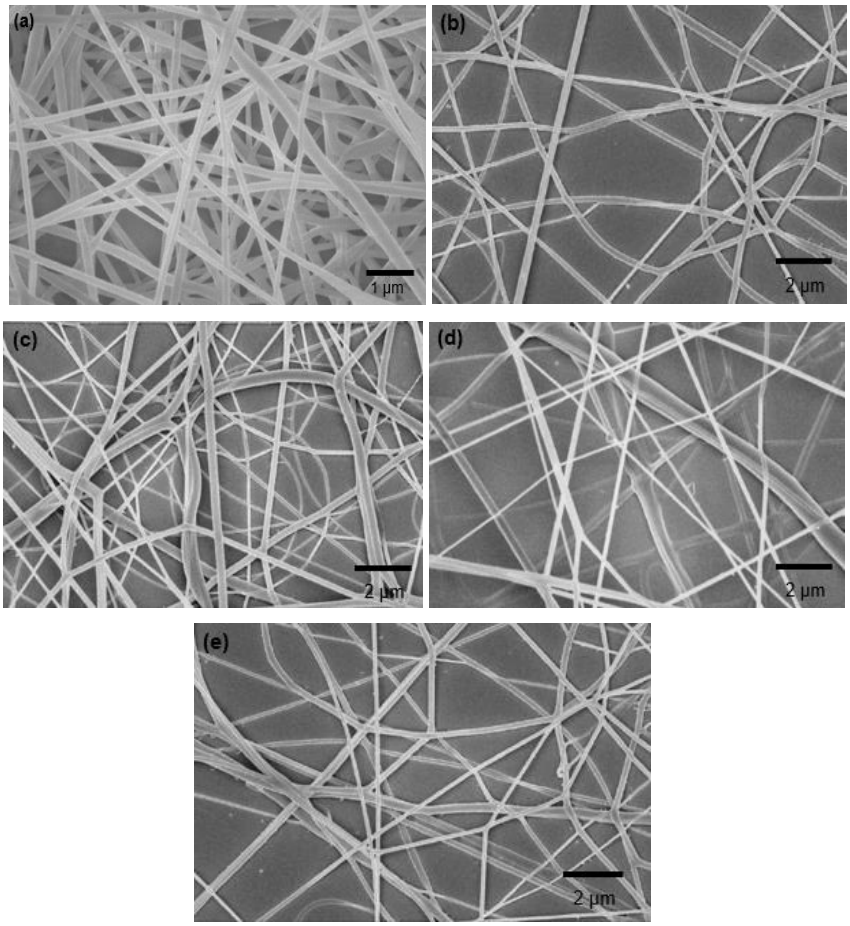

Fig. 3. FESEM images of electrospun fibers for samples (a) 3S7Z, (b) 4S6Z, (c) 5S5Z, (d) 6S4Z and (e) 7S3Z.

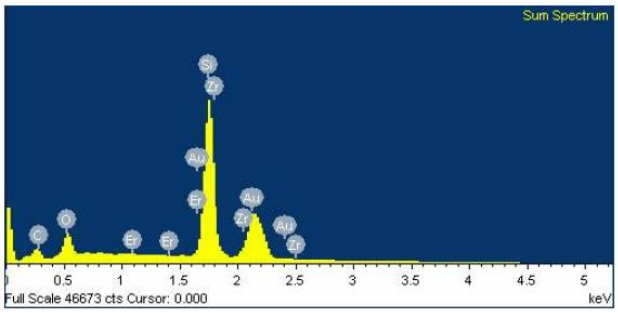

Fig. 4. EDX patterns of calcined electrospun fibers for sample 4S6Z.

Figure 5 displays the XRD patterns of the nanofiber contained different molar ratios of SiO_2-ZrO_2 (70SiO_2-30ZrO_2, 60SiO_2-40ZrO_2, 50SiO_2-50ZrO_2, 40SiO_2-60ZrO_2, 30SiO_2-70ZrO_2)-doped with 0.58 mol% Er^{3+}. The XRD patterns exhibited several diffraction peaks corresponding to the ZrO_2 phase. A broad hump of ~ 22° was due to the amorphous component of the fused silica substrates [9, 27, 28]. Four obvious peaks appeared at approximately 30.6°, 34.9°, 50.5° and 60.8°, which were assigned to the (101), (110), (200) and (211) planes, respectively, and associated with the metastable tetragonal phase of zirconia [29, 30]. All these phases corresponded to a high-temperature state of the annealing process. Pure zirconia demonstrates a tetragonal phase at high temperatures of 1170-2370 °C [31]. However, at low temperatures, the tetragonal phase was present, and this might be correlated to the existence of rare-earth doping [32]. In addition, the rapid thermal annealing of the nanofibers contributed to the generation of tetragonal ZrO_2 [33].

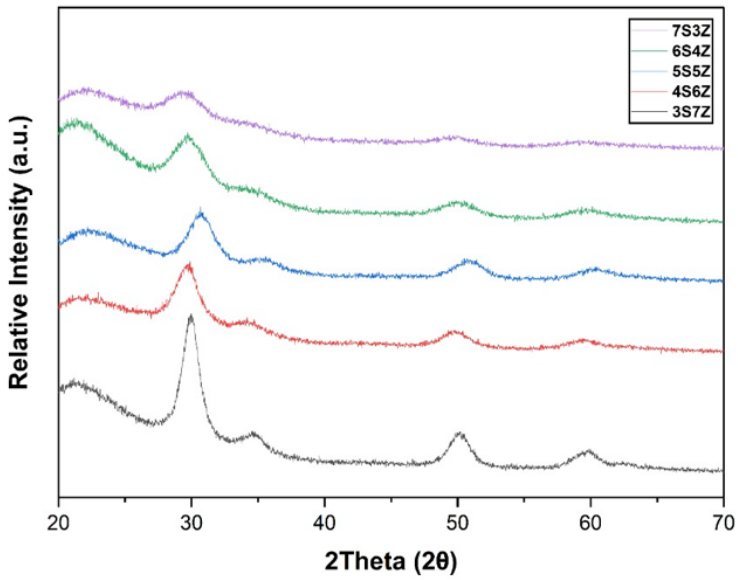

Fig. 5. XRD pattern of Er^{3+}-doped SiO_2-ZrO_2 nanofibers with the different SiO_2-ZrO_2 ratios: 70SiO_2-30ZrO_2 (7S3Z), 60SiO_2-40ZrO_2 (6S4Z), 50SiO_2-50ZrO_2 (5S5Z), 40SiO_2-60ZrO_2 (4S6Z) and 30SiO_2-70ZrO_2 (3S7Z).

As can be seen in Fig. 5, XRD intensity markedly rise with the increase of zirconia amount. This result is evidence of the enhanced crystallinity of the nanofibers. High crystallinity is significant for RE-doped materials as it provides fewer traps and produces longer luminescence [34]. Considering that no alien peaks of the different phases were identified, it can be suggested that the dopant ions had been integrated well into the SiO_2-ZrO_2 network to construct a composite solution. In all XRD patterns (3S7Z, 4S6Z, 5S5Z, 6S4Z and 7S3Z), a diffraction peak located at approximately $2\theta = 30°$ showed a more intense peak than the other peak. This result indicated the preferential orientation of the nanofiber in the direction perpendicular to the substrate surface [35]. Meanwhile, the diffraction peak width became narrower with increasing ZrO_2 content, suggesting that the nanocrystal grain size rose with the increment of ZrO_2 concentration.

As shown in Fig. 5, the zirconia peak for 30 mol% ZrO_2 was weaker when compared with those of the others. This result can be related to the small amounts of crystallites in the samples with low ZrO_2 contents, causing them to be undetected in the XRD studies [35]. Stioa et al. reported that 30% ZrO_2 is prone to exhibit amorphous characteristics in XRD patterns due to the small ZrO_2 particles confined in the amorphous SiO_2 network [1]. This result agrees with previous findings [36] that the 25% ZrO_2 in silicate films showed no crystalline peak of ZrO_2 after the 900 °C rapid thermal annealing. However, the diffraction peak intensity increases coherently with ZrO_2 content.

The FTIR transmittance spectra of the films containing 0.58 mol% Er^{3+}-doped SiO_2-ZrO_2 GC with the molar ratios of $90SiO_2$-$10ZrO_2$, $80SiO_2$-$20ZrO_2$, $70SiO_2$-$30ZrO_2$ and $60SiO_2$-$40ZrO_2$ are presented in Fig. 6. The peaks at 920 and 785 cm^{-1} are ascribed to Si-O-Si symmetrical bending and stretching vibrations, respectively [37, 38]. The peak at 920 cm^{-1} almost disappeared for the $40ZrO_2$ sample because of the low concentration of SiO_2. The peak at 1011 cm^{-1} can be assigned to Si-O-Si asymmetric bond stretching vibration [39, 40]. The characteristics peaks of Si-O-Si vibrations at 1011 and 785 cm^{-1} were less defined in the nanofibres with higher ZrO_2 concentrations. The varying peak intensity in this spectrum indicates that the inclusion of ZrO_2 can alter the connectivity and rigidity of the silica network [41].

A shoulder peak at around 1100 cm^{-1} corresponded to the stretching mode Si-O-bond and a small band at 450 cm^{-1} was appointed to the Si-O-Si bending vibrations [27, 42]. The band associated with the SiO_2 network declined with increasing ZrO_2 concentration. Changes in the infrared intensity were detected by Nogami earlier, who discovered that the silicate structure ruptures when Zr^{4+} is added into the glass matrix [43].

Broad bands at approximately 645 to 660 cm^{-1} were attributed to the tetragonal phase of ZrO_2. Structures in the 500 to 600 cm^{-1} region can be related to the existence of ZrO_x polyhedral, in which the Zr^{4+} ion did not participate with the total anionic framework glass network [41]. Peaks at 970 and 850 cm^{-1} were attributed to Si-O-Zr bond stretching modes [44]. This study agreed with Monte's findings that the existence of Si-O-Zr bonds at bands around 950 and 850 cm^{-1} indicate the stabilization of the tetragonal phase [42]. However, the increment of ZrO_2 content up to 40 mol% can cause the narrow band around 850 cm^{-1} to become broad and reduce in intensity while the peaks at 970 cm^{-1} become less well defined. This phenomenon can cause the breakdown of Si-O-Zr bonds, inducing the phase separation of SiO_2/ZrO_2.

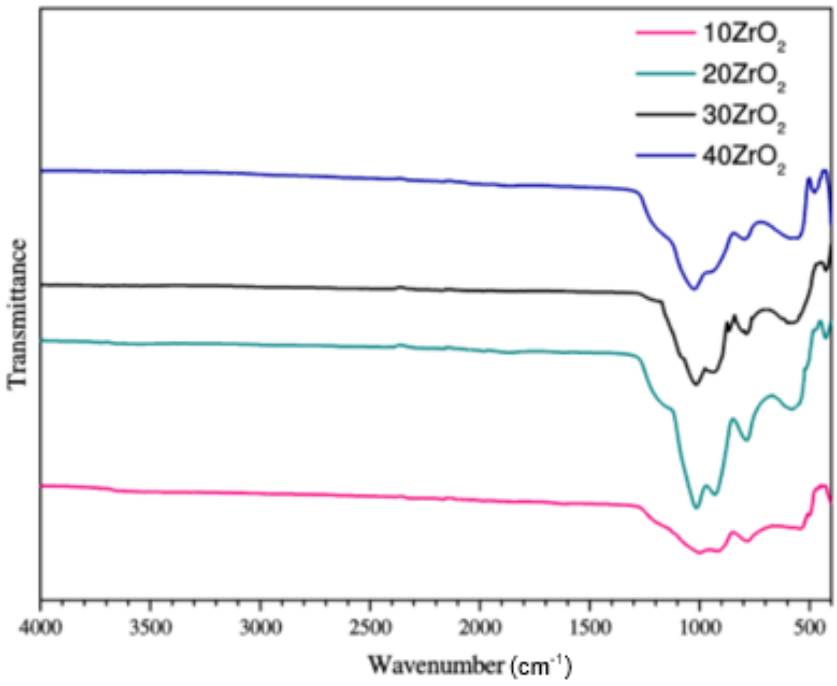

Fig. 6. FTIR spectra of Er^{3+}-doped various ratios of SiO_2-ZrO_2 nanofiber on fused silica substrate.

Bands associated with ZrO_2 tetragonal were also detected at 500 and 700 cm^{-1} [45-47]. Thus, the emergence of bands at approximately 500 and 700 cm^{-1} was assigned to the Zr-O-Zr bond vibration. A sharp band at 500 cm^{-1} was present at high content of ZrO_2 while a broad band at 700 cm^{-1} was associated to the tetragonal ZrO_2. The bands at 500 and 430 cm^{-1} may be due to the phase separation and tetragonal ZrO_2 crystallization from the SiO_2 matrix. [48]. The bands at approximately 3700 and 3000 cm^{-1} can be attributed to the stretching vibrations involving OH groups in silicate glasses [39, 44]. However, the spectra obtained showed the absence of OH - group bands, indicating complete densification of the nanofiber at high annealing temperatures [27, 49]. The existence of OH- must be avoided because it can significantly quench the PL intensity. It can be concluded that zirconia is well dispersed in the silica matrix for molar concentration below 30%.

The photoluminescence spectra of the Er^{3+}-doped SiO_2-ZrO_2 nanofibers with different molar ratios of SiO_2-ZrO_2 are presented in Fig. 7. Each sample produced similar spectra of the emission spectrum with a sharp peak centred at the green and red emission. A changes in the spectral nature of these bands and substantial increase in the spectrum intensity were observed when ZrO_2 content was increased. As reported by Dongwook, the peaky feature in the observed photoluminescence spectra indicates that the synthesized nanofiber contains some nanocrystals [50]. The narrow and sharp peaks indicate the crystallization of Er^{3+} in the local environment [51], which agrees with the XRD findings.

The energy level of Er^{3+} and the emission of ion transition under excitation of 514.5 nm are shown in Fig. 8. The upward arrow denotes as excitation wavelength,

and the downward arrows denote as the radiative Er^{3+} emission. The excitation of 514.5 nm produced red and green emissions. The green PL band, centered at 562 nm is attributed to the $^4S_{3/2} \rightarrow {}^4I_{15/2}$ transition [52] whereas the red luminescence is composed of a few peaks at approximately 645, 650, 655 and 678 nm, which are assigned to $^4F_{9/2} \rightarrow {}^4I_{15/2}$ ion transitions [51]. Stark splitting causes the red emission to be separate into a few peaks of the degenerate 4f levels under the crystal field [53]. In particular, the photoluminescence spectra exhibited well-resolved Stark splitting of radiative emission, indicating that the Er^{3+} ions were in crystalline condition [54]. The inhomogeneous broadening was limited when the local environment of the Er^{3+} ions became more ordered; thus, the luminescence spectra became narrow [55].

The luminescence spectra show that the intensity of Er^{3+} luminescence increased with increasing ZrO_2 content. The addition of ZrO_2 into the silica glass matrix facilitated Er^{3+} ions to disperse homogeneously within the network. As a result, the number of ion clusters reduced, and the luminescence intensity increased [56]. In addition, ZrO_2 has low phonon energy, and this characteristic promotes the reduction in the phonon emission and increases the Er^{3+} ion radiative emission. The 7S3Z samples showed broad spectra with relatively low emission intensity. This result can be ascribed to the high SiO_2 content causing ion clustering because of the rigid structure of SiO_2 that has a strong Si-O-Si covalent bond [57]. This phenomenon leads to the depopulation of the $^4S_{3/2}$ level, which reduces the green emission via cross-relaxation.

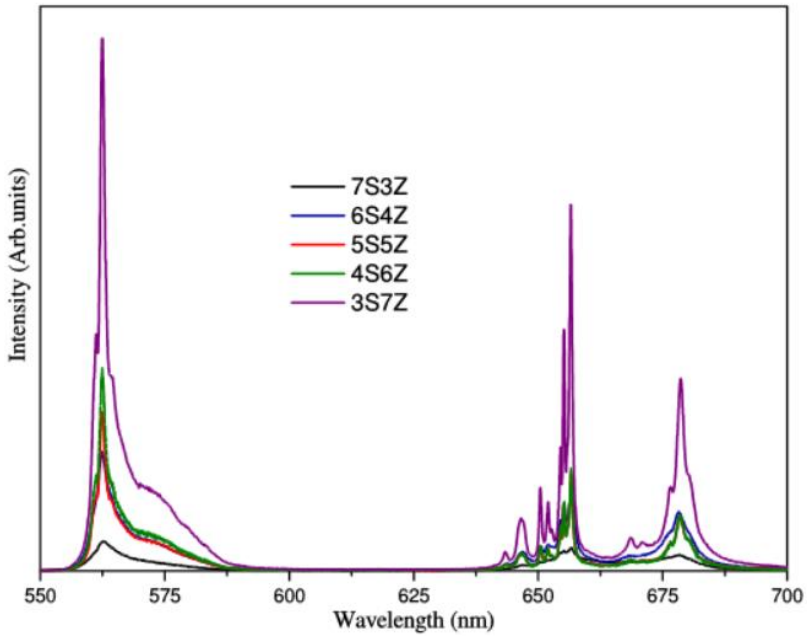

Fig. 7. Photoluminescence spectra of the Er^{3+}-doped samples with various molar ratios of SiO_2:ZrO_2 as assigned by 7S3Z (70SiO_2:30ZrO_2), 6S4Z (60SiO_2:40ZrO_2), 5S5Z (50SiO_2:50ZrO_2), 4S6Z (40SiO_2:60ZrO_2) and 3S7Z (30SiO_2:70ZrO_2).

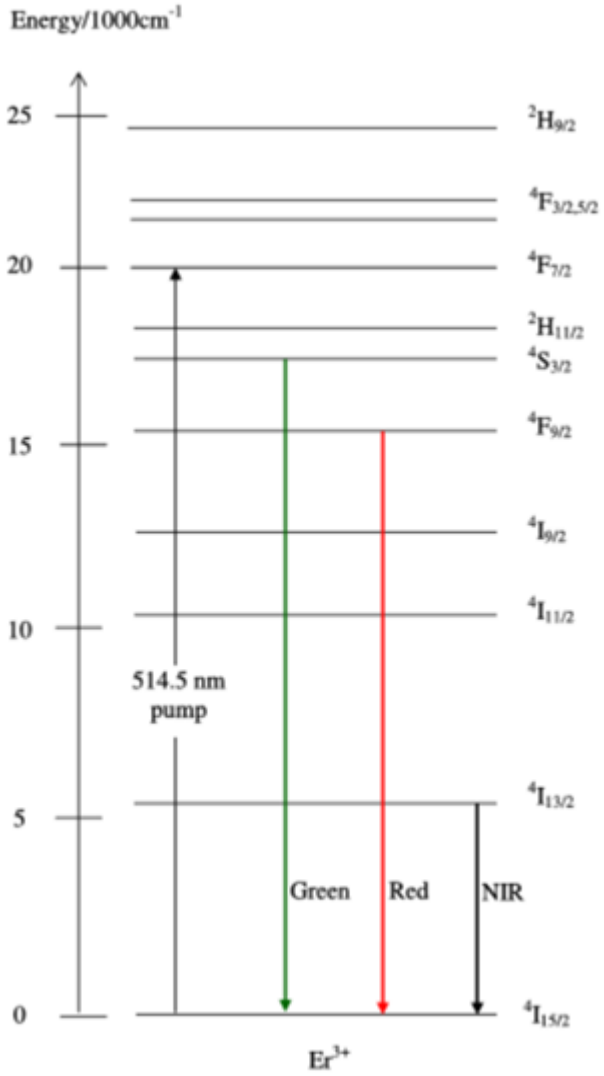

Fig. 8. Energy level diagram of Er^{3+} with the ion transition mechanism under excitation of 514.5 nm.

4. Conclusion

The mixture of ZrO_2 with the SiO_2 host matrix altered the structural, morphological and photoluminescence properties of the fabricated nanofiber. The addition of ZrO_2 positively influenced the solubility of Er^{3+} ions in the GC matrix and the photoluminescence properties of erbium transition. The photoluminescence intensity increased with increasing ZrO_2 content. The narrow and sharp peaks showed the crystallization of the Er^{3+} ion in the local environment. The FTIR spectra obtained showed the absence of the OH^- groups bands, indicating complete densification of the nanofiber at the high annealing temperature. The nanofiber diameter ranged from 130-390 nm depending on the ZrO_2 concentration and calcination temperature.

Acknowledgement

The project was financially supported by the Research Management Center (RMC), Universiti Teknologi MARA (UiTM) through the GIP grant [600-RMC/GIP 5/3 (144/2021)]. The authors would like to thank the Faculty of Applied Sciences, UiTM Shah Alam, Selangor for their sample characterization facilities.

Nomenclatures

Er	Erbium
GC	Glass-ceramic
$\mathcal{PVA}$	Polyvinyl alcohol
SiO_2	Silica
ZrO_2	Zirconium dioxide
EtOH	Ethanol
HCl	Hydrochloric acid
TEOS	Tetraethylorthosilicate

Abbreviations

EDX	Energy dispersive X-ray
FESEM	Field Emission Scanning Electron Microscopy
FTIR	Fourier Transform Infrared
PL	Photoluminescence
XRD	X-Ray Diffraction

References

1. Stoia, M.; Barvinschi, P.; and Barvinschi, F. (2014). Structural and morphologic characterization of zirconia-silica nanocomposites prepared by a modified sol-gel method. *Journal of Crystal Growth*, 401, 462-468.
2. Vařák, P.; Mrazek, J.; Blanc, W.; Aubrecht, J.; Kamradek, M.; and Podrazky, O. (2020). Preparation and properties of Tm-doped SiO_2 -ZrO_2 phase separated optical fibers for use in fiber lasers. *Optical Materials Express*, 10(6), 1383-1390.
3. Kumar, A.; Singhal, S.; Aggarwal, S.; Badoni, R.P.; and Sharma, A. K. (2018). Influence of synthetic approach of SiO_2-ZrO_2 materials. *Catalysis for Sustainable Energy*, 5, 34-40.
4. Persson, C.; Unosson, E.; Ajaxon, I.; Engstrand, J.; Engqvist, H.; and Xia, W. (2012).Nano grain sized zirconia-silica glass ceramics for dental applications. *Journal of European Ceramic Society*, 32, 4105-4110.
5. Wang, Y.; Hu, D.; Li, J.; and Wu, S. (2013). Study on optical properties of SiO_2/ZrO_2 and ZrO_2/SiO_2 bilayer films prepared by sol-gel method. *Optik*, 124, 2421-2423.
6. Isogai, M.; Veber, A.; de Ligny, D.; Cicconi, M. R.; and Hayakawa, T. (2018). Devitrification behavior of sol-gel derived ZrO_2-SiO_2 rare-earth doped glasses: Correlation between structural and optical properties. *Ceramics*, 1, 274-286.
7. De Pablos-Martin, A.; Ferrari, M.; Pascual, M. J.; and Righini, G. C. (2015). Glass-ceramics: A class of nanostructured materials for photonics. *La Rivista del Nuovo Cimento*, 38(7-8), 311-369.

8. Razaki, N. I.; Kamil, S. A.; and Abd-Rahman, M. K. (2021). Preparation and characterization of SiO_2-ZrO_2: Er^{3+}/Yb^{3+} thin film deposited on fused silica and silicon wafer substrate via sol-gel dip coating technique. *AIP Conference Proceedings*, 2332, 120003.
9. Kamil, S. A.; Chandrappan, J.; Murray, M.; Steenson, P; Krauss, T. F.; and Jose G. (2016). Ultrafast laser plasma doping of Er^{3+} ions in silica-on-silicon for optical waveguiding applications. *Optics Letters*, 41(20), 4684-4687.
10. Hua, Y.; and Yu, J. S. (2021). Strong green emission of erbium(III)-activated La_2MgTiO_6 phosphors for solid-state lighting and optical temperature sensors. *ACS Sustainable Chemistry and Engineering*, 9, 5105-5115.
11. Lo Faro, M. J.; Leonardi, A. A.; Priolo, F.; Fazio, B.; Miritello, M.; and Irrera, A. (2020).Erbium emission in Er:Y_2O_3 decorated fractal arrays of silicon nanowires. *Scientific Reports*, 10, 12854.
12. Polman A. (1997). Erbium implanted thin film photonic materials. *Applied Physics Reviews*, 82(1), 1-39.
13. Farias, P. M.; Santos, B. S.; Chaves, C. R.; Figueiredo, R.C.B.Q.; Ferreira, R. C.; and Fontes, A. (2008).. Hybrid organic/II-VI quantum dots: highly luminescent nanostructures for bioimaging. *Proceedings of Molecular Probes for Biomedical Applications II.* California, USA, 68670G.
14. Ali, U.; Zhou, Y.; Wang, X.; and Lin T. (2011). *Nanofibers-Production, Properties and Functional Applications*. Intech.
15. Wu, X.; and Tong, L. (2013). Optical microfibers and nanofibers. *Nanophotonics*, 2(5-6), 407-428.
16. Kong, Y. C.; Yu, D. P.; Zhang, B.; Fang, W.; and Feng, S. Q. (2001). Ultraviolet-emitting ZnO nanowires synthesized by a physical vapor deposition approach. *Applied Physics Letters*, 78(4), 407-409.
17. Bhardwaj, N.; and Kundu, S. C. (2010). Electrospinning: A fascinating fiber fabrication technique. *Biotechnology Advances*, 28, 325-347.
18. Liu, L. X.; Ma, Z. W.; Xie, Y. Z.; Su, Y. R.; Zhao, H. T.; Zhou, M.; Zhou, J. Y.; Li, J.; and Xie, E. Q. (2010). Photoluminescence of rare earth^{3+} doped uniaxially aligned HfO_2 nanotubes prepared by sputtering with electrospun polyvinylpyrolidone nanofibers as templates. *Journal of Applied Physics*, 107, 024309.
19. Zhang, Z.H.; Long, Y.Z.; Yin, H.X.; Sun, B.; Zheng, J.; Zhang, H.D.; Ji, X. M.; and Gu, C.Z. (2012). Electrospun fluorescein/polymer composite nanofibers and their photoluminescent properties. *Chinese Physics B*, 21(9), 097805.
20. Ji, L.; Saquing, C.; Khan, S. A.; and Zhang X. (2008). Preparation and characterization of silica nanoparticulate-polyacrylonitrile composite and porous nanofibers. *Nanotechnology*, 19, 085605.
21. Mwiiri, F. K.; and Daniels, R. (2020). Influence of PVA molecular weight and concentration on electrospinnability of birch bark extract-loaded nanofibrous scaffolds intended for enhanced wound healing Francis. *Molecules*, 25, 4799.
22. Petras, D.; Slobodian, P.; Pavlínek, V.; Sáha, P.; and Kimmer, D. (2011). The effect of PVAc solution viscosity on diameter of PVAc nanofibres prepared by technology of electrospinning. *AIP Conference Proceeding*, 1375, 312-319.

23. Haider, A.; Haider, S.; and Kang, I. K. (2018). A comprehensive review summarizing the effect of electrospinning parameters and potential applications of nanofibers in biomedical and biotechnology. *Arabian Journal of Chemistry*, 11, 1165-1188.
24. Tarus, B.; Fadel, N.; Al-Oufy, A.; and El-Messiry, M. (2016). Effect of polymer concentration on the morphology and mechanical characteristics of electrospun cellulose acetate and poly (vinyl chloride) nanofiber mats. *Alexandria Engineering Journal*, 55, 2975-2984.
25. Doshi, J.; and Reneker, D. H. (1995). Electrospinning process and applications of electrospun fibers. *Journal of Electrostatic*, 35,151-60.
26. Tunc, T.; and Uslu I. (2013). Fabrication and characterization of boron doped yttria-stabilized zirconia nanofiber. *Polymer Engineering and Science*, 53(5), 963-969.
27. Gonçalves, R. R.; Guimarães, J. J.; Ferrari, J. L.;, Maia, L. J. Q.; and Ribeiro, S. J. L. (2008). Active planar waveguides based on sol-gel Er^{3+}-doped SiO_2-ZrO_2 for photonic applications: morphological, structural and optical properties. *Journal of Non-Crystalline Solids*, 354, 4846-4851.
28. Fishlock, S. J.; Pu, S. H.; Bhattacharya, G.; Han, Y.; McLaughlin, J.; McBride J. W.; Chong, H. M. H. and Shea, S. J. O. (2018). Micromachined nanocrystalline graphite membranes for gas separation. *Carbon*, 138, 125-133.
29. Kamil, S. A.; Zulkepli, N.; Nawi, I. N. M.; Razaki, N. I.; and Abd-Rahman, M. K. (2019). Optical and structural properties of Er^{3+}-doped SiO_2-ZrO_2 glass-ceramic thin film. *Journal of Physics: Conference Series*, 1349, 012035.
30. Wang, J.; Yin, W.; He, X.; Wang, Q.; Guo, M.; and Chen, S. (2016). Good biocompatibility and sintering properties of zirconia nanoparticles synthesized via vapor-phase hydrolysis. *Scientific Reports*, 6, 35020.
31. Mihai, L. L.; Parlatescu, I.; Gheorghe, C.; Andreescu, C.; Bechir, A.; Pacurar, M.; and Cumpata, C. N. (2016). In vitro study of the effectiveness to fractures of the aesthetic fixed restorations achieved from zirconium and alumina. *Revista de Chimie*, 65(6), 725-729.
32. Liu, R.; Ji, L.; Xu, Y.; Ye, F.; and Jia, F. (2016). Catalytic performance and SO_2 tolerance of tetragonal-zirconia-based catalysts for low-temperature selective catalytic reduction. *Journal of Materials Research*, 31(17), 2590-2597.
33. Ramesh, S.; Zulkifli, N.; Tan, C. Y.; Wong, Y. H.; Tarlochan, F.; Ramesh, S.; Teng, W. D.; Sopyan, I.; Bang, L. T.; and Sarhan, A. D. (2018). Comparison between microwave and conventional sintering on the properties and microstructural evolution of tetragonal zirconia. *Ceramic International*, 44(8), 8922-8927.
34. Atabaev, T. S.; Kurisu, M.; Konishi, K.; and Hong, N. H. (2014). Concentration-dependent optical properties of erbium doped zirconia nanocrystals. *American Journal of Nanoscience and Nanotechnology*, 2,13-6.
35. Joy, K.; Maneeshya, L. V.; Thomas, J. K.; and Thomas, P. V. (2012). Effect of sol concentration on the structural, morphological, optical and photoluminescence properties of zirconia thin films. *Thin Solid Films*, 520, 2683-2688.
36. Lucovsky, G.; Rayner, G. B.; Kang, D.; Hinkle, C. L; and Hong, J. G. (2004). A spectroscopic study distinguishing between chemical phase separation with

different degrees of crystallinity in Hf(Zr) silicate alloys. *Applied Surface Science*, 234, 429-433.

37. Monte, F. D.; Larsen, W.; and Mackenzie, J. D. (2000). Stabilization of tetragonal ZrO_2 in ZrO_2-SiO_2 binary oxides. *Journal of the American Ceramic Society*, 83(3), 628-634.
38. Waseem, M.; Mustafa, S.; Naeem, A.; Shah, K. H.; Shah, I.; and Ul-Haque, I. (2009). Synthesis and characterization of silica by sol-gel method. *Journal of Pakistan Materials Society*, 3(1), 19-21.
39. Siddiqui, M.R. H.; Al-Wassil, A. I.;, Al-Otaibi, A. M.; and Mahfouz, R. M. (2012). Effects of precursor on the morphology and size of ZrO_2 nanoparticles, synthesized by sol-gel method in non-aqueous medium. *Material Research*. 15(6), 986-989.
40. Mohamed, E. A.; and Ibrahim, A. A. (2014). Influence of reaction conditions on sol-gel process producing SiO_2 and SiO_2-P_2O_5 gel and glass. *New Journal of Glass and Ceramics*, 4, 42-47.
41. Pickup, D. M.; Mountjoy, G.; Wallidge, G. W.; Newport, J.; and Smith, M. E. (1999). Structure of $(ZrO_2)_x(SiO_2)_{1-x}$ xerogels (x= 0.1, 0.2, 0.3 and 0.4) from FTIR , ^{29}Si and ^{17}O MAS NMR and EXAFS. *Physical Chemistry Chemical Physics*, 1, 2527-2533.
42. del Monte, F.; Larsen, W.; and Mackenzie, J. D. (2000). Chemical interactions promoting the ZrO_2 tetragonal stabilization in ZrO_2-SiO_2 binary oxides. *Journal of the American Ceramic Society*, 83(6), 1506-1512.
43. Lee, S. W.; and Condrate, R. A. (1988). The infrared and Raman spectra of ZrO_2-SiO_2 glasses prepared by a sol-gel process. *Journal of Materials Science*. 23, 2951-2159.
44. Neumayer, D. A.; and Cartier, E. (2001). Materials characterization of ZrO_2-SiO_2 and HfO_2-SiO_2 binary oxides deposited by chemical solution deposition. *Journal of Applied Physics*, 90(4), 1801-1808.
45. Štefanić, G.; Musić, S.; Popović, S.; and Sekulić, A. (1997). FT-IR and laser Raman spectroscopic investigation of the formation and stability of low temperature t-ZrO_2. *Journal of Molecular Structure*, 408-409, 391-394.
46. Yu, Y.; Wang, X.; Cao, Y.; and Hu, X. (2001). Study on the structure and properties of ZrO_2 buffer layers on stainless steel by XRD, IR and AES. *Applied Surface Science*, 172, 260-264.
47. Chinchamalatpure, V. R.; Chore, S. M.; Patil, S. S.; and Chaudhari, G. N. (2012). Synthesis and electrical characterization of ZrO_2 thin films on Si(100). *Journal of Modern Physics*, 3, 69-73.
48. Ferrari, M.; Armellini, C.; Ronchin, S.; Rolli, R.; Duverger, C.; Monteil, A.; Balu, N.; and Innocenzi, P. (2000). Influence of the Er^{3+} content on the luminescence properties and on the structure of Er_2O_3-SiO_2 xerogels. *Journal of Sol-Gel Science and Technology*, 19, 569-572.
49. Seco, A. M.; Gonçalves, M. C.; and Almeida, R. M. (2000). Densification of hybrid silica-titania sol-gel films studied by ellipsometry and FTIR. *Materials Science and Engineering B*, 76, 193-199.
50. Shin D. (2006). Photoluminescence of erbium-doped silica-based waveguide film via flame hydrolysis deposition and aerosol doping. *Journal of Ceramic Processing Research*, 7(4), 379-383.

51. Gonçalves, R. R.; Messaddeq, Y.; Chiasera, A.; Jestin, Y.; Ferrari, M.; and Ribeiro S. J. L. (2008). Erbium-activated silica-zirconia planar waveguides prepared by sol-gel route. *Thin Solid Films*, 516, 3094-3097.
52. Stręk, W.; Deren, P.J.; Maruszewski, K.; Pawlik, E.; Wojcik, W.; Malashkevich, G. E.; and Gaishun, V. I. (1998). Spectroscopic properties of erbium doped silica glasses obtained by sol-gel method. *Journal of Alloys and Compounds*, 275-277, 420-423.
53. Wang, J.; Shi, Z. Q.; Shi, Y.; Pu, L.; Pan, L. J.; Zhang, R.; Zheng, Y. D.; Tao, Z. S.; and Lu, F. et al. (2009). Broad excitation of Er luminescence in Er-doped HfO_2 films. *Applied Physics A*, 94, 399-403.
54. Lai, L. J.; Chu, T. C.; Lin, M. I.; and Lin, Y. K. (2007). Photoluminescence of thin films ZrO_2:Er^{3+} excited by soft X-ray. *Solid State Communications*, 144, 181-184.
55. Jestin, Y.; Armellini, C.; Chiappini, A.; Chiasera, A.; Ferrari, M.; Goyes, C.; Montagna, M.; Moser, E.; Nunzi Conti, G.; Pelli, S.; Retoux, R.; Righini, G. C.; and Speranza, G.(2007). Erbium activated HfO_2 based glass-ceramics waveguides for photonics. *Journal of Non-Crystalline Solids*, 353, 494-497.
56. Auzel, F.; and Goldner, P. (2001). Towards rare-earth clustering control in doped glasses. *Optical Materials*, 16, 93-103.
57. Afify, N. D.; Dalba, G.; Rocca, F.; and Ferrari, M. (2007). Er^{3+}-activated SiO_2 -based glasses and glass-ceramics: from structure to optimisation. *Physics and Chemistry of Glasses - European Journal of Glass Science and Technology Part B*, 48(4), 229-34.